Coupling impedance of an in-vacuum undulator: Measurement, simulation, and analytical estimation

Victor Smaluk* and Richard Fielder
Diamond Light Source, Oxfordshire OX11 0DE, United Kingdom

Alexei Blednykh
Brookhaven National Laboratory, Upton, New York 11973, USA

Guenther Rehm
Diamond Light Source, Oxfordshire OX11 0DE, United Kingdom

Riccardo Bartolini
Diamond Light Source, Oxfordshire OX11 0DE, United Kingdom
John Adams Institute, University of Oxford, Oxford OX1 3RH, United Kingdom
(Received 9 April 2014; published 25 July 2014)

One of the important issues of the in-vacuum undulator design is the coupling impedance of the vacuum chamber, which includes tapered transitions with variable gap size. To get complete and reliable information on the impedance, analytical estimate, numerical simulations and beam-based measurements have been performed at Diamond Light Source, a forthcoming upgrade of which includes introducing additional insertion device (ID) straights. The impedance of an already existing ID vessel geometrically similar to the new one has been measured using the orbit bump method. The measurement results in comparison with analytical estimations and numerical simulations are discussed in this paper.

DOI: 10.1103/PhysRevSTAB.17.074402 PACS numbers: 29.20.-c, 29.27.Bd

I. INTRODUCTION

In-vacuum undulators with a small vertical gap are the major contributors to the total coupling impedance of modern synchrotron light sources. So, one of the important design issues of the vacuum chambers for in-vacuum insertion devices (IDs) is the minimization of their impedance. In the framework of the forthcoming Diamond Light Source upgrade, additional IDs will be installed to increase the capacity of the facility. It is proposed to convert some of the double-bend achromat (DBA) lattice cells into a double-DBA, with a new ID straight between the two achromats [1]. The new lattice allows the introduction of a 2-m long in-vacuum ID with a 5 mm full gap without impacting the limiting aperture of the existing ring and with negligible impact on emittance and energy spread. A standard U21 in-vacuum undulator is assumed for the new beam line, although a cryogenic permanent magnet undulator is also under consideration.

A series of analytical estimations, numerical simulations and beam-based measurements have been performed to get complete and reliable information on the ID coupling impedance and to study the possibility of decreasing the length of tapered transitions. For a variable-gap in-vacuum ID, this is the first-time comparison of measured impedance with analytical estimations and numerical simulations. The vacuum chamber of the ID section has a complex geometry including tapers, foils, transition between elliptic and flat cross sections, etc., see Fig. 1. It is therefore impossible to derive accurate analytical formulas for the impedance of the whole chamber. Full 3D computer simulation of such a big and complicated structure is quite difficult too because huge memory and processor time are required, especially if we need to know the wakefields induced by rather short (few mm) bunches. Nevertheless, analytical formulas for the geometric and resistive-wall impedances of a simplified flat taper model are available, so we can estimate the impedance as a function of gap to compare with the measurement results. For the same flat rectangular tapered structure, wakefield simulations have been carried out using finite-difference simulation codes GdfidL [2] and CST Particle Studio [3].

II. COMPUTER SIMULATIONS AND ANALYTICAL FORMULAS

A. Model for calculation of geometric impedance

Here we present the simulation results, which are compared with analytical estimates. Total impedance of a vacuum chamber can be considered as a sum of the

*victor.smalyuk@diamond.ac.uk

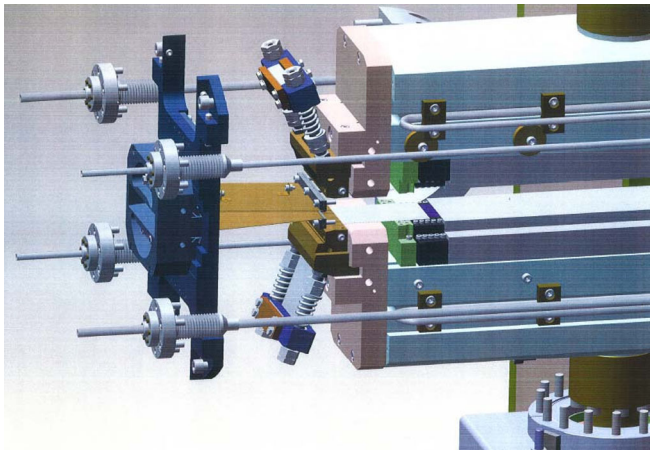

FIG. 1. Layout of the ID tapered transition without vacuum enclosure.

geometric and the resistive-wall components. The geometric impedance is completely determined by the chamber shape. The vacuum chamber of the ID includes flat tapered transitions with a variable vertical aperture from $2b = 5$ mm (ID closed) up to $2b = 30$ mm (ID open). The entrance and exit vertical aperture of the ID vacuum chamber is $2d = 18.4$ mm, the length of the tapered transition is $l = 108.5$ mm, and the width of parallel copper plates forming the transition is $w = 84$ mm.

Figure 2 shows the model used for the wakefield simulation, the structure is a rectangular tapered collimator if $b < d$, whereas it is considered as a rectangular tapered cavity if $b > d$. The taper length l and the entrance and exit vertical half-aperture d are fixed and are unchangeable during all the simulations performed. The half-gap b is varied in the range from 2.5 mm up to 15 mm. The separation length $l_{\mathrm{ID}} = 500$ mm between two tapers was chosen long enough to be certain that the simulation results are independent of l_{ID}. Although the actual length of the undulator is 2480 mm, this simplification is possible because the contribution of the flat part to the geometric broadband impedance is negligible, as it was checked by the wakefield simulations performed with varied length of the central part.

B. Longitudinal impedance

A set of formulas for calculation of low-frequency geometric impedance of tapered transitions can be found in [4]. These formulas have been derived using perturbation theory applied to the field equations; the applicability condition is $b \ll w \ll l$. Note that the requirement $w \ll l$ is not strictly satisfied in our case, because $w = 84$ mm and $l = 108.5$ mm. The longitudinal impedance is assumed to be inductive at low frequencies, the frequency ω is considered as a small parameter.

If the beam pipes connected to the transition are identical at both ends, the perturbation theory gives the formula of normalized impedance $Z_{\parallel}/n$:

$$\frac{Z_{\parallel}}{n} = -i\frac{Z_0\omega_0}{4\pi c}\int_{-\infty}^{\infty}(g')^2 F\left(\frac{g}{w}\right)dz, \tag{1}$$

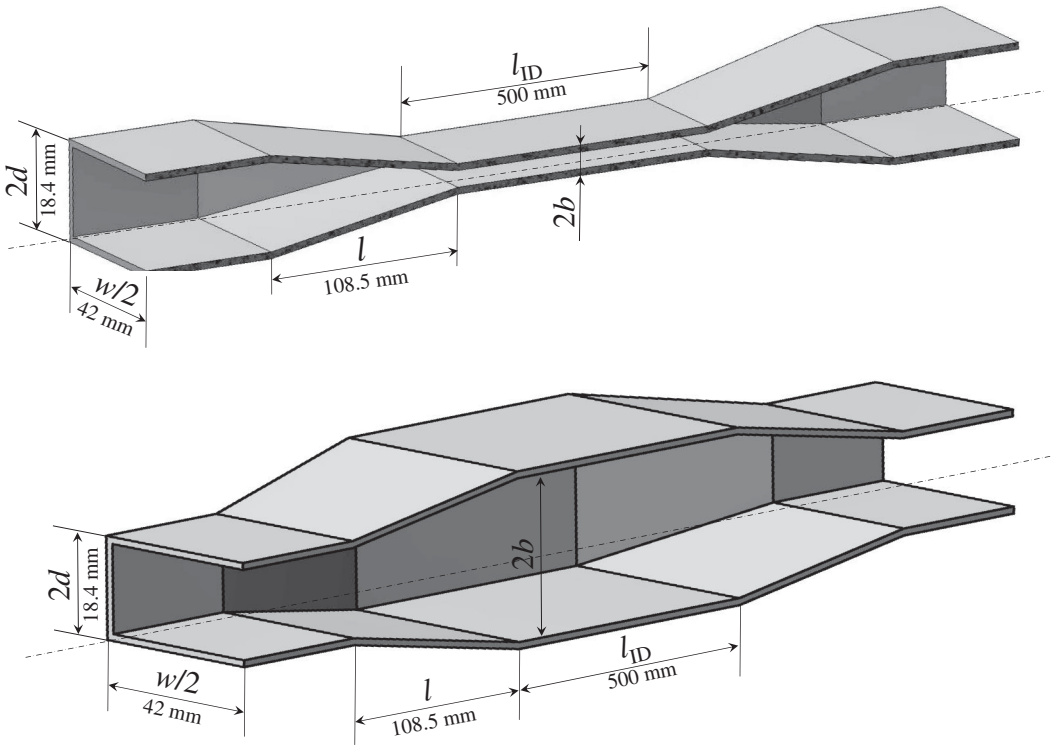

FIG. 2. Simplified model for wakefield simulation: rectangular tapered collimator (upper) and rectangular tapered cavity (lower).

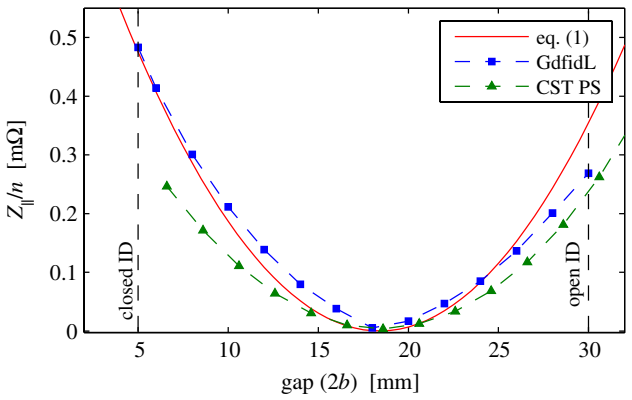

FIG. 3. Longitudinal normalized impedance—gap dependence.

where $g' = dg/dz$, $g(z)$ is the vertical gap profile along the z axis, w is the full width, $Z_0 \simeq 377\Omega$ is the free space impedance, $n = \omega/\omega_0$, ω_0 is the cyclic revolution frequency ($\omega_0 = 2\pi \cdot 533.8$ kHz for Diamond). The function $F(\frac{g}{w})$ is defined as

$$F(x) = \sum_{m=0}^{\infty} \frac{1}{2m+1} \operatorname{sech}^2 \phi_m \tanh \phi_m, \qquad (2)$$

and the argument of hyperbolic functions in (2) is $\phi_m = (2m+1)\frac{\pi x}{2}$. For these calculations, the infinite sum in (2) has been truncated at 100 because there is no further dependence on the number of terms in our case.

Figure 3 shows the normalized impedance $Z_\parallel/n$ of one ID section (two tapered transitions) as a function of the gap height $2b$. There is the impedance (1) in comparison with the results of computer simulation performed using the 3D codes CST PARTICLE STUDIO and GDFIDL.

As one can see, the impedance calculated by CST PARTICLE STUDIO is underestimated in comparison with the GDFIDL data, if $b < d$ (collimator mode). The problem is CST PS contains two indirect integration methods. The older and well established "indirect testbeams" can only be used for cavitylike structures where none of the structure intrudes closer to the beam than the entrance and exit beam pipes. The newer method "indirect interfaces" is intended to address this and allow collimatorlike structures as well. However, testing shows that this method does not always produce good results, if meshing is not fine enough. The indirect interfaces method requires higher mesh density than the indirect testbeams for the same accuracy of simulation. In our case, the integration step size was 50 μm for the GDFIDL simulation, and the minimum possible step size for the CST simulation was 40 μm (limited by the computer capabilities). So a possible reason of the discrepancy between CST and GDFIDL could be the insufficiently fine mesh for the CST simulation.

The normalized impedance $Z_\parallel/n$ as a function of the taper width w is presented in Fig. 4, both the analytical

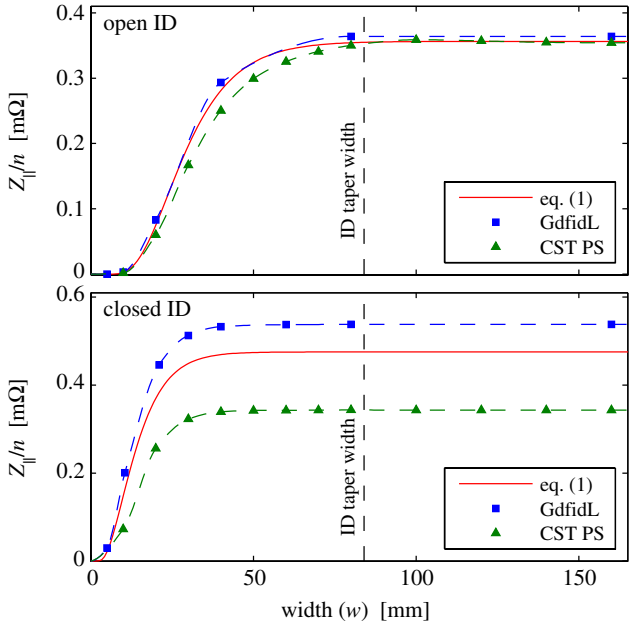

FIG. 4. Longitudinal normalized impedance—width dependence calculated for $b = 15$ mm (upper plot) and for $b = 2.5$ mm (lower plot).

estimation (1) and computer simulation are shown. There are data calculated for $b = 15$ mm (upper plot) and for $b = 2.5$ mm (lower plot). The other parameters are $d = 9.2$ mm, $l = 108.5$ mm. As one can see, if the taper width exceeds a certain value, the impedance becomes independent on the width. For our case, the full width w of ID taper (dashed vertical line in Fig. 4) is above this threshold. For the collimatorlike structure (closed ID), the CST and GDFIDL data diverge by the reason described above.

C. Transverse impedance and kick factor

For a chamber with mirror symmetry relative to the $x = 0$ and $y = 0$ planes, the horizontal Z_x and vertical Z_y impedances can be approximated by a sum of dipole $Z_{x,yD}$ and quadrupole $Z_{x,yQ}$ components:

$$\begin{aligned} Z_x(\omega, x_1, x_2) &\simeq x_1 Z_{xD}(\omega) + x_2 Z_{xQ}(\omega), \\ Z_y(\omega, y_1, y_2) &\simeq y_1 Z_{yD}(\omega) + y_2 Z_{yQ}(\omega), \end{aligned} \qquad (3)$$

where x_1, y_1 are the transverse coordinates of a driving particle acting on a following particle with x_2, y_2 transverse coordinates. Placing the following particle on axis ($y_2 = 0$) we can express the dipole vertical impedance by calculation of the wakefields using the simulation codes GDFIDL and CST PARTICLE STUDIO. Placing the driving and following particles off axis ($y_1 = y_2 > 0$), we can express total geometric impedance Z_y, which can be compared with the measured data.

To compare the results of measurements and simulations, we use the kick factor

$$k_\perp = \frac{1}{2\pi}\int_{-\infty}^{\infty} Z_\perp(\omega)h(\omega)d\omega, \tag{4}$$

where $k_\perp, Z_\perp$ are horizontal k_x, Z_x or vertical k_y, Z_y; $h(\omega) = \lambda(\omega)\lambda^*(\omega)$ is the bunch power spectrum, $\lambda(\omega)$ is the Fourier transform of beam linear density $\lambda(t)$. For a Gaussian beam and frequency-independent impedance corresponding to the inductive regime,

$$k_\perp = \frac{\mathrm{Im}Z_\perp c}{2\sqrt{\pi}\sigma_s}, \tag{5}$$

where σ_s is the rms bunch length.

In case of a wide taper ($b \ll w \ll l$) and a long bunch $\sigma_s \gg b$ (inductive regime), perturbation theory applied to the field equations [4] gives the vertical dipole Z_{yD} and quadrupole Z_{yQ} impedance:

$$Z_{yD} = -i\frac{\pi}{4}Z_0 w\int_{-\infty}^{\infty}\frac{(g')^2}{g^3}G_1\left(\frac{g}{w}\right)dz, \tag{6}$$

$$Z_{yQ} = -Z_{xQ} = -i\frac{\pi}{4}Z_0\int_{-\infty}^{\infty}\frac{(g')^2}{g^2}G_2\left(\frac{g}{w}\right)dz, \tag{7}$$

where

$$G_1(x) = x^3\sum_{m=0}^{\infty}(2m+1)\mathrm{csch}^2\phi_m\coth\phi_m, \tag{8}$$

$$G_2(x) = x^2\sum_{m=0}^{\infty}(2m+1)\mathrm{sech}^2\phi_m\tanh\phi_m, \tag{9}$$

$g(z)$ is the vertical gap profile along the z axis, and the argument of hyperbolic functions in (8) and (9) is $\phi_m = (2m+1)\frac{\pi x}{2}$.

In Fig. 5, we plot the quadrupole kick factor as computed by the GDFIDL code with 25 μm step size (squares) and 50 μm step size (circles) vs the kick factor calculated using formulas (5) and (7). The bunch length was $\sigma_s = 7$ mm. As one can see, the GDFIDL data converge well to the analytical results by reducing the step size for the tapered collimator structure. A good agreement was also found between the results for the tapered cavity structure even with coarse step size.

Figure 6 shows the quadrupole kick factor calculated by GDFIDL as a function of the taper full width w. The wakefield simulations were carried out with 25 and 50 μm step size, $\sigma_s = 7$ mm, fixed $b = 2.5$ mm, $d = 9.2$ mm, $l = 108.5$ mm, $l_{ID} = 500$ mm and variable w. As can be seen the quadrupole kick factor has a maximum knob before saturation at full width $w \simeq 10$ mm, both for the formula and GDFIDL simulation. Figure 6 also shows that the GDFIDL simulation results tend to the formula, when the step size decreases.

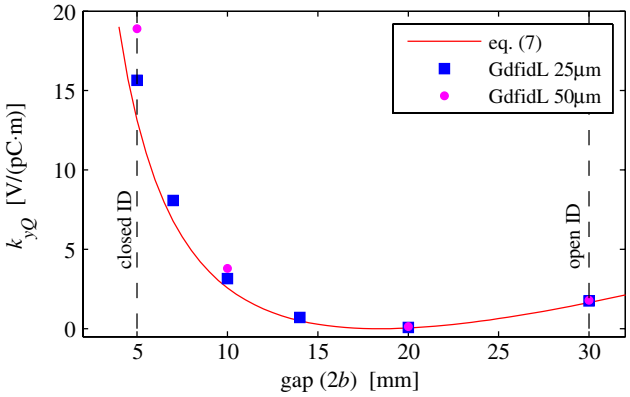

FIG. 5. Quadrupole kick factor—gap dependence.

Figure 7 shows the dipole kick factor calculated by GDFIDL as a function of the taper full width w for $b = 15$ mm (upper plot) and for $b = 2.5$ mm (lower plot). The wakefield simulation was carried out with 50 μm step size, $\sigma_s = 7$ mm, $d = 9.2$ mm, $l = 108.5$ mm, $l_{\mathrm{ID}} = 500$ mm. As can be seen the dipole kick factor grows almost linearly first and after that reaches saturation. The kick factor has a maximum knob at full width $w \simeq 80$ mm. Some research was done on flat tapered transitions [5] with geometric parameters, which are differed from the current geometry. The kick factor has a knob with some maximum value in all considered cases before it becomes independent on width. For small width w, the dipole kick factor from GDFIDL agrees with the solid line in Fig. 7, representing the kick factor (5) calculated with Z_{yD} from formula (6).

Since the actual taper width $w = 84$ mm is close to the saturation threshold and the vertical impedance cannot be approximated by (6), another model has been chosen to estimate the vertical kick factor for comparison with the measurement results. Formulas published in [6] have been derived using the boundary perturbation method assuming

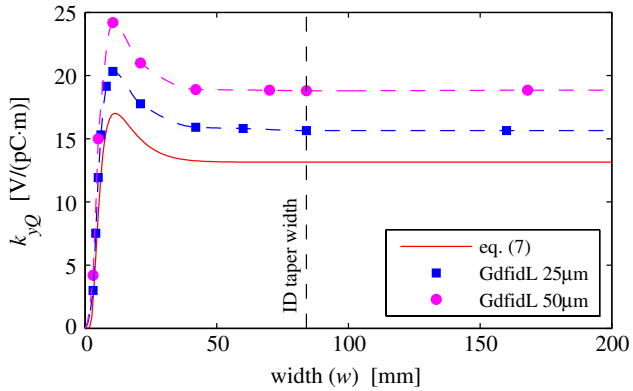

FIG. 6. Quadrupole kick factor—width dependence calculated for $b = 2.5$ mm.

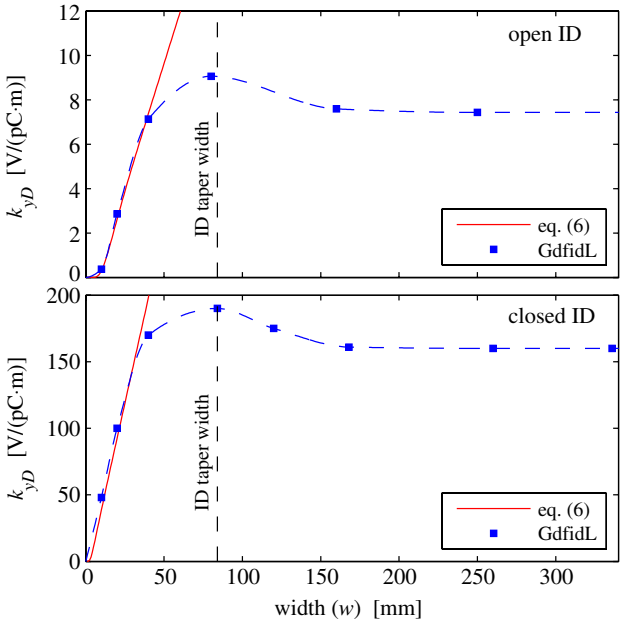

FIG. 7. Dipole vertical kick factor—width dependence calculated for $b = 15$ mm (upper plot) and for $b = 2.5$ mm (lower plot).

a taper of infinite width, $w \to \infty$. The frequency-dependent vertical impedance is

$$Z_y(k) = -i\frac{Z_0}{2\pi b_0} \times \int_{-\infty}^{\infty} \frac{\xi^2}{\sinh^2\xi} \sum_{n=0}^{\infty} \delta_n \frac{H(k_n,k) + H(k_n,-k)}{2ik_n b_0} d\xi, \tag{10}$$

where $k = \omega/c$ is the wave number, $2b_0 = b + d$, $\delta_n = 1$ if $n = 0$ and $\delta_n = 2$ if $n > 0$,

$$k_n b_0 = \sqrt{(kb_0)^2 - \xi^2 - (\pi n)^2}, \tag{11}$$

$$H(p,k) = \int_{-\infty}^{\infty}\int_{-\infty}^{z_1} S'(z_1)S'(z_2)e^{i(p+k)(z_1-z_2)}dz_1 dz_2, \tag{12}$$

$S' = dS/dz$, $S(z) = \frac{g(z)-b_0}{b_0}$, $g(z)$ is the vertical gap profile along the z axis.

For a range of the ID gaps, the vertical kick factor has been calculated by formula (4) using the impedance (10) and the bunch power spectrum $h(\omega) = \exp(-\omega^2\sigma_s^2/c^2)$. The analytically calculated kick factor k_{yD} as a function of gap height $2b$ is presented in Fig. 8 (solid line) in comparison with the results of CST PARTICLE STUDIO simulation (green triangles) and GDFIDL simulations performed with the 25 μm step (blue squares) and 50 μm step (magenta circles).

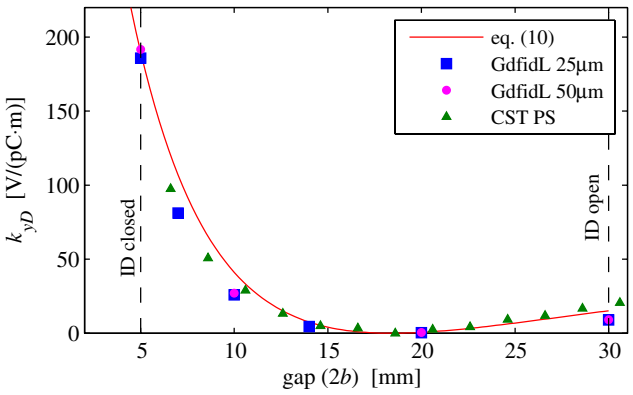

FIG. 8. Dipole vertical kick factor—gap dependence.

D. Resistive wall impedance and kick factor

In spite of the copper foil covering the magnets, resistive-wall impedance of the long (2 m) undulator with a narrow gap (5 mm if closed) makes considerable contribution into the kick factor, comparable with the geometric one. Formulas to calculate the resistive-wall impedance have been derived analytically for the round and flat vacuum chambers [7]. For a vertically displaced beam in a round chamber, the transverse impedance per unit length is

$$Z_y^{\mathrm{rnd}}(\omega) = \frac{\mathrm{sign}\omega + i}{\pi b^3}\sqrt{\frac{c\mu_r Z_0}{2\omega\sigma_c}}\frac{1 + 3(y/b)^2}{[1-(y/b)^2]^3}, \tag{13}$$

where y is the beam offset, b is the inner chamber radius; μ_r and σ_c are the relative permeability and conductivity of the chamber material, respectively; Z_0 is the free space impedance.

For a vertically displaced beam in a flat chamber formed by two infinitely wide plates with the distance $2b$ between them, the impedance per unit length is

$$Z_y^{\mathrm{flat}}(\omega) = \pi\frac{\mathrm{sign}\omega + i}{8b^3}\sqrt{\frac{c\mu_r Z_0}{2\omega\sigma_c}}\frac{1 + \frac{\pi y}{2b}\tan\frac{\pi y}{2b}}{\cos^2\frac{\pi y}{2b}}. \tag{14}$$

For a beam placed in the center of vacuum chamber,

$$Z_\perp^{\mathrm{flat}}(\omega) = \frac{\pi^2}{8}Z_\perp^{\mathrm{rnd}}(\omega). \tag{15}$$

The resistive-wall kick factors (4) of the flat and round copper vacuum chambers calculated for a Gaussian bunch with 7-mm length using the formulas (13) and (14) are shown in Fig. 9 as functions of the chamber aperture $2b$. The resistive-wall kick factor contributed by two tapered transitions is less than 10 V/(pC m) at worst (closed ID).

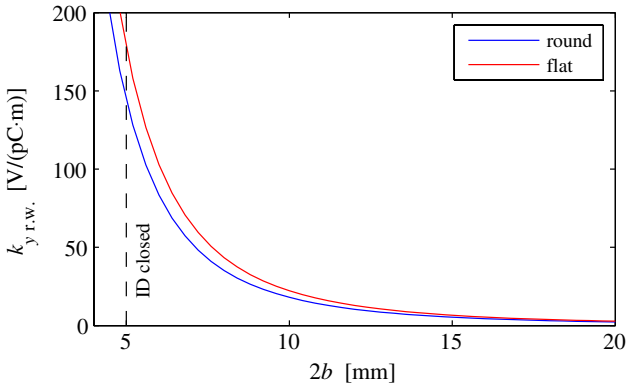

FIG. 9. Resistive-wall kick factor.

III. BEAM-BASED MEASUREMENT

To estimate the contribution of the new ID section into the total broadband impedance of the ring, the kick factor of the existing ID16 geometrically similar to the new one has been measured using the orbit bump method. The measurement technique has been developed and realized first at Budker Institute of Nuclear Physics [8]. Later, similar techniques were used at APS [9], ELETTRA [10], and ESRF [11]. The method is based on the fact that an off-axis beam passing through the vacuum chamber section with a nonzero transverse impedance is deflected by the wakefields. If a bunched beam is displaced from the equilibrium orbit at the location of the transverse impedance, the beam-impedance interaction results in a kick of the beam transverse momentum $\Delta y'$ proportional to the beam position y_0 at the impedance location:

$$\Delta y' = \frac{q}{E/e} k_\perp y_0, \tag{16}$$

where q is the bunch charge, E is its energy, and $k_\perp$ is the kick factor (4).

If two closed orbits are measured with different beam intensity, the orbit deviation caused by the beam-impedance interaction is

$$\Delta y(s) = \frac{\Delta q}{E/e} k_\perp y_0 \frac{\sqrt{\beta(s)\beta(s_0)}}{2\sin \pi\nu} \cos[|\mu(s) - \mu(s_0)| - \pi\nu], \tag{17}$$

where s_0 is the transverse impedance location, Δq is the bunch charge variation, ν is the betatron tune, β is the beta function, and μ is the betatron phase advance. This wavelike orbit deviation can be measured using beam position monitors (BPMs), and the wave amplitude is proportional to the kick factor at the bump location.

To reduce the systematic error caused by intensity-dependent behavior of the BPM electronics, this error is also measured and then subtracted. First of all, after the initial correction of the orbit to zero, two reference orbits y_{01} and y_{02} are measured at the high and low values of beam current. Then, after creating the orbit bump, again two orbits y_1 and y_2 are measured at the same beam current values. In the four-orbit combination $\Delta y = (y_2 - y_1) - (y_{02} - y_{01})$, the systematic error is eliminated, as well as the bump itself.

Figures 10 and 11 show the orbit deviation (17) measured with the same gap height of 5 mm (ID closed), but the first measurement has been done with the bunch charge difference $\Delta q = 1.3$ nC and the bump height $y_0 = 1$ mm, whereas for the second measurement $\Delta q = 2.1$ nC and $y_0 = 1.5$ mm. In these graphs, the red dots represent average values of ten consecutive measurements of beam position and the error bars—standard deviations. The solid line is the model orbit deviation calculated using formula (17) and the Twiss functions from the linear model of the magnet optics. As one can see, the amplitude of orbit wave increases with the product $y_0 \Delta q$ of the bump height and bunch charge difference, in agreement with (17).

Accuracy δy of the orbit measurement depends on the resolution δy_{BPM} of a single BPM as $\delta y = \delta y_{\mathrm{BPM}}/\sqrt{N}$, where $N \gg 1$ is the number of BPMs. In spite of the small magnitude (few μm) of orbit deviation to be observed, the resolution of Diamond BPMs turns out to be sufficient for this measurement. In our case, the pure BPM noise resulting in uncorrelated beam position uncertainty is not expected to be that large. So we can suspect that there were real orbit fluctuations (correlated motion due to a single or

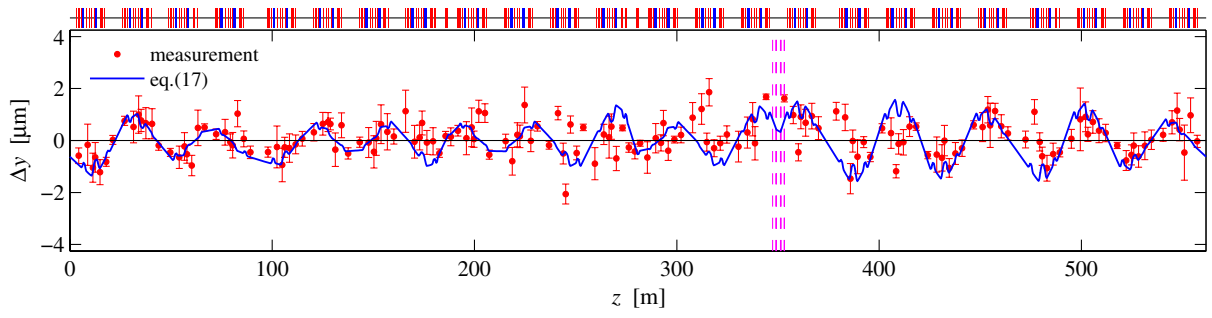

FIG. 10. Orbit deviation: $\Delta q = 1.3$ nC, $y_0 = 1$ mm.

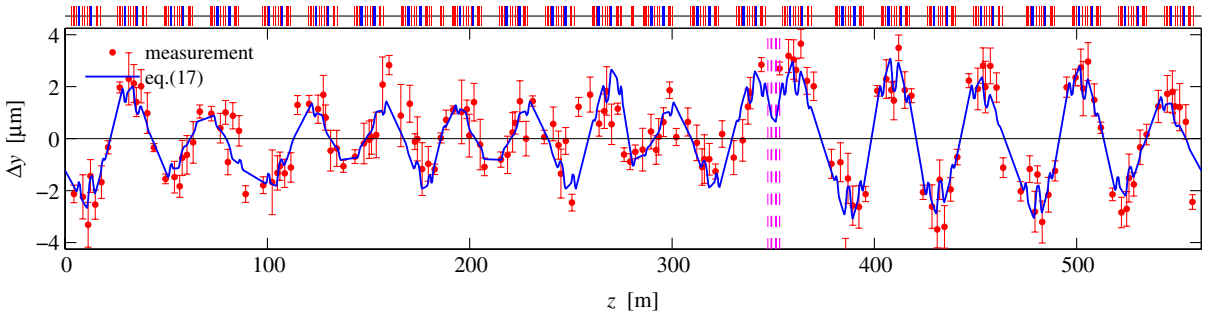

FIG. 11. Orbit deviation: $\Delta q = 2.1$ nC, $y_0 = 1.5$ mm.

several unstable correctors), which might have some impact on the error estimate. As a result, the error bars in Figs. 10 and 11 represent the integral error of the orbit measurement including both BPM noise and beam position fluctuations.

Note that formula (17) was derived for a short bump, with the beta function $\beta(s_0)$ and betatron phase advance $\mu(s_0)$ assumed constant through the bump length. As for the real measurements, the bump length is a couple of meters, and the beta function and betatron phase has been taken averaged over the bump length. Besides the variable-gap tapers, the section covered by the bump includes few more considerable contributors to the vertical kick factor: two step transitions from the 72×20 racetrack chamber to the 82×38 octagonal chamber (all cross sections in mm) and two electrostatic beam position monitors with bellows. Thus the measured orbit deviation represents effects of all impedances located within the bump.

IV. DISCUSSION OF RESULTS

The vertical kick factor of ID16 has been measured for seven values of the ID gap height. Note that a single-bunch effect was measured and the orbit deviation (17) is proportional to the single bunch charge variation. But due to the limitation of a single-bunch current in the Diamond storage ring, the measurements were carried out with a special beam filling pattern: five equally spaced bunches with 1–2 mA single-bunch current. This was done to improve the signal-to-noise ratio, because the BPM sensitivity is proportional to the average beam current. We assume that the bunch-to-bunch distance (about 375 ns) was large enough to let the short-range wakefields disappear, and there was no bunch-to-bunch interaction. The rms bunch length at the 1–2 mA range of bunch current is 6.5–8 mm [12]. The bunch lengthening introduced by closing the ID is negligible.

The measurement and simulation results are summarized in Fig. 12 representing the vertical kick factor k_y as a function of the ID gap $2b$. The geometric kick factor k_y is a sum of the dipole k_{yD} and quadrupole k_{yQ} ones. For the long (2 m) in-vacuum ID with the small (5 mm) gap, the resistive-wall contribution to the kick factor cannot be neglected, so it has been estimated separately and added to the analytical and simulation results for comparison with the measured data. The total measured kick factor is shown in red dots with error bars. The simulated results by CST PARTICLE STUDIO and the GDFIDL code are green triangles and blue squares, respectively. The solid line is the analytical calculation performed using formulas (10) and (7).

Since the analytical calculations and the wakefield simulations have been carried out for the simplified model shown in Fig. 2, the contribution of other components of the ID vessel were not taken into account. Nevertheless, there is a significant gap-independent part of the kick factor introduced by the above-mentioned step transitions and beam position monitors. In Fig. 12, the constant kick factor estimated as 180 V/(pC m) has been added to the analytical and simulation data for better fit of the measured kick factor. Using the well-known formula of low-frequency impedance of a step transition $Z_\perp = i\frac{Z_0(d-b)}{\pi b^2}\frac{d^2-b^2}{d^2+b^2}$, we can roughly estimate the kick factor contributed by two transitions from the racetrack chamber ($b = 10$ mm) to the octagonal chamber ($d = 19$ mm): $k_y \simeq 150$ V/(pC m). The rest of the constant kick factor

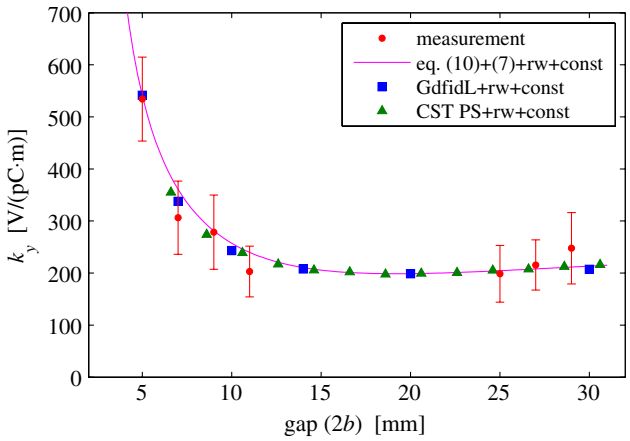

FIG. 12. Vertical kick factor vs ID gap.

can be contributed by the electrostatic BPMs, bellows and resistive walls.

As one can see in Fig. 12, the formulas (10)–(12) and the simulation performed using CST PARTICLE STUDIO and GDFIDL represent the gap-dependent behavior of the kick factor quite consistently with the measured data. Also we can conclude that the vertical kick factor does not depend on the taper width, if it exceeds a certain threshold. This is illustrated by a quite good agreement between the measurements, numerical simulations performed for the taper width of 84 mm and the formulas derived for the infinitely wide taper.

The total vertical kick factor of the Diamond storage ring has been estimated using the broadband impedance model, the parameters of which were obtained from the beam-based measurements. Taking into account the geometric and resistive-wall impedance, we can assume that for the bunch length of 7 mm the total vertical kick factor is about 7 $\mathrm{kV}/(\mathrm{pC\,m})$ if all in-vacuum IDs are open, and it is about 11 $\mathrm{kV}/(\mathrm{pC\,m})$ if the IDs are closed. Thus, according to the measurement, computer simulation and analytical computation described in this paper, the contribution of one in-vacuum ID section into the total vertical kick factor is about 3.5% for the open ID and about 4.5% for the closed ID.

ACKNOWLEDGMENTS

The authors would like to thank S. Krinsky for very useful discussions. This work was supported by DOE Contract No. DE-AC02-98CH10886.

[1] R. Bartolini, C. P. Bailey, M. P. Cox *et al.*, in *Proceedings of the 4th International Particle Accelerator Conference, IPAC-2013, Shanghai, China, 2013* (JACoW, Shanghai, China, 2013), MOPEA068.

[2] W. Bruns, The GDFIDL Electromagnetic Field simulator, http://www.gdfidl.de/.

[3] CST-Computer Simulation Technology, CST PARTICLE STUDIO, http://www.cst.com/Content/Products/PS/Overview.aspx.

[4] G. Stupakov, Phys. Rev. ST Accel. Beams **10**, 094401 (2007).

[5] A. Blednykh and S. Krinsky (private communication).

[6] S. Krinsky, Phys. Rev. ST Accel. Beams **8**, 124403 (2005).

[7] A. Piwinski, Report No. DESY-94-068, Hamburg, 1994.

[8] V. Kiselev and V. Smaluk, "A Method for Measurement of Transverse Impedance Distribution along Storage Ring," in *Proceedings of the 4th European Workshop on Beam Diagnostics and Instrumentation for Particle Accelerators (DIPAC 99)*, edited by B. G. Martlew and R. J. Smith (Daresbury Laboratory, Warrington, United Kingdom, 2000), p. 191.

[9] L. Emery, G. Decker, and J. Galayda, in *Proceedings of the 19th Particle Accelerator Conference, Chicago, IL, 2001* (IEEE, Piscataway, NJ, 2001), TPPH070.

[10] E. Karantzoulis, V. Smaluk, and L. Tosi, Phys. Rev. ST Accel. Beams **6**, 030703 (2003).

[11] T. Perron, L. Farvacque, and E. Plouviez, in *Proceedings of the 9th European Particle Accelerator Conference, Lucerne, 2004* (EPS-AG, Lucerne, 2004), WEPLT085.

[12] R. Bartolini, R. T. Fielder, and C. A. Thomas, in *Proceedings of the 4th International Particle Accelerator Conference, IPAC-2013, Shanghai, China, 2013* (Ref. [1]), TUPWA052.